



Near real-time multi-GNSS orbits, clock and observable-specific biases at Wuhan University

Xiaolong Xu¹ · Junqiang Li¹ · Jing Guo¹ · Chao Yang¹ · Qile Zhao^{1,2}

Received: 15 May 2024 / Accepted: 19 August 2024 / Published online: 1 September 2024
© The Author(s), under exclusive licence to Springer-Verlag GmbH Germany, part of Springer Nature 2024

Abstract

Precise orbit, clock and observable-specific phase bias products play a pivotal role in facilitating precise point positioning (PPP) with ambiguity resolution (AR). The model and strategy used to generate Wuhan University Multi-GNSS (WUM) hourly updated ultra-rapid products is summarized in this study. A refined iteration of the block-to-block operation method is introduced, which demonstrates a substantial increase in efficiency, achieving enhancements of 13-fold and 29-fold for Central Processing Unit and Graphics Processing Unit platforms, respectively. Subsequently, a pre-integration approach is introduced for numerical orbit integration, resulting in a noticeable improvement of efficiency ranging from 6 to 28 times. To enhance the solution strength and precision, a single-differenced-based ambiguity fixing method is explored in our routine processing, which improves for all the satellites, except for GLONASS, and multi-GNSS products are released with a 1-h latency. The orbit assessment is conducted through a comparative analysis with International GNSS Service (IGS) and the Wuhan University Multi-GNSS Combined orbits. The three-dimensional precision of the near real-time orbits reaches 2.4 cm, 4.6 cm, 3.8 cm, and 4.9 cm for GPS, GLONASS, Galileo, and BDS3 MEO satellites, respectively. Regarding IGSO satellites of BDS and QZSS, the corresponding values range between 11.4 cm and 15.7 cm. In contrast, the GEOS of BDS and QZSS exhibit comparatively inferior performance, demonstrating consistencies of 234.7 cm and 70.9 cm, respectively. The validation of the near real-time products is performed utilizing PPP-AR. The statistical analysis across a global network of 340 stations with 20 days reveals a wide-lane fixing rate exceeding 91.1% for multi-GNSS, accompanied by a narrow-lane fixing rate of approximately 97.0%. The PPP-AR solution demonstrates the accuracy of 1.6 mm, 1.7 mm, and 5.0 mm in the east, north, and up directions for IGS weekly solutions, respectively. The results are promising and further confirm that the products are effective.

Keywords GNSS · Real-time orbit · High performance computing · Observable-specific bias

Introduction

The International GNSS Service (IGS) operates as a voluntary institution committed to delivering the utmost precision in global navigation satellite system (GNSS) related products. Wuhan University (WHU) is contributing to the ultra-rapid, rapid product lines. As an analysis center (AC) of multi-GNSS experiment (MGEX), WHU has consistently submitted final products since 2013 and near real-time

(NRT) products since 2019. More than 120 satellites have already been launched into orbit for service of positioning, navigation and timing (PNT). Positioning accuracy, reliability and convergence time have been greatly enhanced, which drives the development of real-time services. Centimeter-level accuracy can be achieved with real-time precise point positioning (PPP) in a global scale by geodetic-type receivers, and the ambiguity resolution (AR) can further improve the accuracy to millimeter-level (Ge et al. 2008; Geng et al. 2019b). Distinguishing from the relative positioning measurement, high-performance orbit, clock, and observable-specific bias (OSB) products are the prerequisite.

Currently, there are two distinct methods for the generation of real-time orbits: the epoch-wise filtering techniques (Bertiger et al. 2020; Dai et al. 2019; Kazmierski et al. 2018; Takasu 2013), and the so-called ultra-rapid solutions (Lutz

✉ Jing Guo
jingguo@whu.edu.cn

¹ GNSS Research Center, Wuhan University, No. 129 Luoyu Road, Wuhan 430079, China

² Collaborative Innovation Center of Geospatial Technology, No. 129 Luoyu Road, Wuhan 430079, China

et al. 2016; Männel et al. 2020). For filtering methods, the orbit states are estimated as stochastic parameters in process, and the random characteristics of the force model between epochs are considered. Lou et al. (2022) reviewed and summarized the issues for the real-time filtering precise orbit determination (POD), and promising performance can be expected during the period of maneuvers and eclipse seasons. But the major issues including stability, accuracy, reliability, and reconvergence for the orbit generation are still challenges due to the unavoidable interruption of the real-time data stream. For comparison, the ultra-rapid orbit is widely used owing to its feasibility and reliability of routine processing at most IGS ACs (Tang et al. 2023). The regular ultra-rapid GPS and GLONASS orbit products of IGS are released every 6 h with a latency of 3 h (Springer and Hugentobler 2001). Deutsches GeoForschungsZentrum (GFZ) starts to provide the multi-GNSS products with 3-h update rate since 2015 (Deng et al. 2016). To refine the orbit prediction model, several research, including Choi et al. (2013); Nowak et al. (2023), suggested that optimum ranges of arc lengths are about 42–48 h for the determination of multi-GNSS orbits. In addition, the solar radiation pressure (SRP) is a key issue for orbit estimation and prediction (Duan et al. 2019; Prange et al. 2016), where the hybrid strategy of combining both empirical and physical models with accurate metadata shows better performance (Nowak et al. 2023). Besides, the prediction of the Earth orientation parameter (EOP) also affects the real-time orbit quality and is still an open issue (Lutz et al. 2016; Śliwińska et al. 2022).

Integer ambiguity fixing is a crucial procedure in GNSS data processing, which is important on both the server and user side. The orbit can be improved with undifferenced ambiguity resolution (Deng et al. 2022; Geng et al. 2022). On the user side, the phase-bias products play a pivotal role in recovering the integer property of ambiguity, thereby enhancing the solution of single station positioning. Several phase-bias models, uncalibrated phase delay (UPD) (Ge et al. 2008), integer clock model (Laurichesse et al. 2009), and decoupled clock model (Collins et al. 2010), are used for PPP-AR. Various methodologies are employed in the generation of phase-bias products, which inevitably introduces complexity to user-side with corrections from ACs. To ensure the interoperability of bias products from ACs, the OSB product is recommended by the IGS PPP-AR working group. The ACs can correct the bias straightforwardly, and users of IGS products can easily handle the bias products (Schaer 2016).

The generation of these corrections at ACs poses a challenge in near real-time patterns, particularly with a globally covered massive network. Expedited GNSS data processing has been obtained more and more concern. In general, the utilization of sufficient sites with better distribution will contribute to improving performance in the orbit solution.

However, this requires a compromise in terms of processing time. Hence, numerous strategies have been proposed to mitigate the time consumption associated with data processing in massive networks. Herring (2004) partitioned the network into sub-networks, and subsequently combined the normal equations (NEQ) of each sub-network to obtain the final estimation (Steigenberger et al. 2006; Tan et al. 2022). The number of parameters per subnetwork is notably reduced, particularly in relation to ambiguities and receiver clocks. The overlapping stations is requisite for connecting the subnetworks, leading to a potential overoptimization in the estimation of these stations. Meanwhile, the recovery of massive integer ambiguities is the main computational burden. Blewitt et al. (2010) devised the carrier-range approach, where the conversion of carrier phase to carrier-range is achieved through double-differenced integer ambiguities based on fixed-point theorems. Furthermore, PPP with integer ambiguity resolution was also used to obtain the carrier-range by fixing the undifferenced ambiguity directly (Chen et al. 2014). The utilization of carrier-range measurements facilitates a more efficient determination of orbit and clock estimations. Nevertheless, it is not a suitable option for NRT solutions for the procedure of carrier-range converting. Moreover, the algorithm employed for the elimination and recovery of inactive parameters, widely adopted within the GNSS community as proposed by Ge et al. (2006), proves time-consuming due to its reliance on element-by-element operations. Chen et al. (2022) demonstrated that computational efficiency can be threefold accelerated through the implementation of a multi-thread guided scheduling scheme and optimizing cache memory traffic. The application of QR factorization and matrix-reduction step algorithms accelerate the calculation of the square root information filter (SRIF) (Barbu et al. 2018; Gong et al. 2018), allowing the clock estimation with 82 globally distributed stations at one epoch to be solved in less than 1 s. Furthermore, Li et al. (2017) and the Gravity Recovery Object-Oriented Programming System (GROOPS) software employ parallel computing methods (Li et al. 2019; Mayer-Gürr et al. 2021). Besides, the epoch-parallel processing strategy is used to diminish the orbit update latency, wherein the processing tasks are partitioned into several sub-sessions (Tang et al. 2023). The utilization of low-rate data also contributes to a reduction in processing time, as demonstrated by Li et al. (2019).

In this study, we focus on the methodologies and strategies employed in the generation of near real-time Wuhan University Multi-GNSS (WUM) solution, aiming at improving the accuracy and computational efficiency of orbit, clock, and OSB products. Following the introduction, this paper delves into enhanced methodologies for undifferenced ambiguity resolution, parameter solving and orbit integration. These advancements are integral to the NRT orbit determination and its practical application. Afterward, the strategy used for

routine product generation are presented. Following this, an evaluation is conducted on the performance of the proposed algorithms, along with an assessment of the NRT orbit and positioning solutions. Finally, a comprehensive conclusion is drawn.

Methodology

In this section, the methodologies used for the generation of NRT orbit, clock and OSB with massive network are described in detail. Firstly, the method of the single-difference ambiguity fixing as well as the mapping of dual-frequency phase OSB are introduced, which is critical for improving orbit, clock, and PPP-AR application. Then, the optimized algorithms, parameter elimination and numerical orbit integration, used for the generation of NRT products are demonstrated.

Observable-specific phase biases

The first-order ionospheric delay can be effectively mitigated using ionosphere-free (IF) observations. Subsequently, the undifferenced (UD) measurement equation for code and carrier-phase is expressed as

$$\left\{ \begin{array}{l} \rho_{IF,a}^k = \frac{f_i^2}{f_i^2 - f_j^2} \rho_{i,a}^k - \frac{f_j^2}{f_i^2 - f_j^2} \rho_{j,a}^k \\ \quad = R_a^k + c\delta t_a - c\delta t^k + m_a^k T_a + d_{\rho_{IF,a}} - d_{\rho_{IF}}^k + \varepsilon_{\rho_{IF}} \\ \phi_{IF,a}^k = \frac{f_i^2}{f_i^2 - f_j^2} \phi_{i,a}^k - \frac{f_j^2}{f_i^2 - f_j^2} \phi_{j,a}^k \\ \quad = R_a^k + c\delta t_a - c\delta t^k + m_a^k T_a + d_{\phi_{IF,a}} - d_{\phi_{IF}}^k + \lambda_i N_{IF,a}^k + \varepsilon_{\phi_{IF}} \end{array} \right. \quad (1)$$

where $\rho_{IF,a}^k$ and $\phi_{IF,a}^k$ represent the code and phase IF observation in length; f_i and f_j denote the frequencies corresponding to the respective signals; R_a^k denotes the station-satellite geometric distance; T_a is the zenith tropospheric delay (ZTD) with mapping function m_a^k ; δt_a and δt^k are the receiver and satellite clock offsets; here $\lambda_i = c/f_i$ represents the wavelength of the frequency i , and c denoting the speed of light in vacuum; $d_{\rho_{IF,a}}$ and $d_{\phi_{IF,a}}$ are the hardware biases of IF combination at station a for code and phase, whereas $d_{\rho_{IF}}^k$ and $d_{\phi_{IF}}^k$ are those at satellite k . $N_{IF,a}^k$ denotes the integer ambiguity parameter; $\varepsilon_{\rho_{IF}}$ and $\varepsilon_{\phi_{IF}}$ are the noises of code and phase measurements. The ambiguity of IF combination is expressed with

$$\lambda_i N_{IF,a}^k = \lambda_w \lambda_n N_{w,a}^k / \lambda_j + \lambda_n N_{n,a}^k \quad (2)$$

where $\lambda_w = c/(f_i - f_j)$ and $\lambda_n = c/(f_i + f_j)$ are the wide-lane and narrow-lane wavelengths. $N_{w,a}^k = N_{i,a}^k - N_{j,a}^k$ and $N_{n,a}^k = N_{i,a}^k$ represent wide-lane and narrow-lane ambiguities.

As indicated by Eq. (1), parameters involving phase hardware bias, ambiguity, and clock cannot be effectively separated due to linear correlation. Consequently, the hardware bias will be assimilated into the IF ambiguity estimate. For the resolution of wide-lane ambiguity, the Melbourne-Wübbena combination is used due to the relatively longer wavelength of wide-lane (Melbourne 1985). To mitigate the influence of receiver hardware bias, a between-satellites single-difference calculation is applied at the common site. The fractional part, considered as wide-lane UPD (UPD_w), can be extracted with fixing the wide-lane ambiguity. The narrow-lane ambiguity is derived with the IF ambiguity estimate and the fixed wide-lane ambiguity. Commonly, the bootstrapping method with a suitable threshold is capable of processing in batch mode (Dong and Bock 1989), and the narrow-lane UPD (UPD_n) can be extracted subsequently. The variation of UPD_w is quite stable, which is always regarded as constant within the scope of solution (Ge et al. 2008). Regarding UPD_n , its stability over time is compromised due to disturbances errors in observations, orbit models, and clock. However, the UPD_n parameters are decomposed as the time-invariable portions and time-variable portions (Geng et al. 2019b), where the time-variable parts can be assimilated into the satellite clock. Therefore, the UPD_n parameters is estimated as a constant over a defined period. A between-satellite single-difference calculation is processed for the separation of receiver UPD, and then satellite-specific parameters can be obtained by imposing a zero-mean condition on the corrections for all involved satellites. In addition, the daily wide-lane and narrow-lane UPD can be converted to the observable-specific biases with consideration of code OSB correction, and expressed as

$$\begin{pmatrix} OSB_{p_i} \\ OSB_{p_j} \end{pmatrix} = \begin{pmatrix} \frac{f_i}{f_i - f_j} & -\frac{f_j}{f_i - f_j} \\ \frac{f_i^2}{f_i^2 - f_j^2} & -\frac{f_j^2}{f_i^2 - f_j^2} \end{pmatrix}^{-1} \begin{pmatrix} \widehat{UPD}_w \\ UPD_n \end{pmatrix} \quad (3)$$

$$\widehat{UPD}_w = UPD_w + \frac{f_i}{f_i + f_j} OSB_{c_i} + \frac{f_j}{f_i + f_j} OSB_{c_j} \quad (4)$$

where OSB_{p_i} , OSB_{p_j} , OSB_{c_i} and OSB_{c_j} are the observable-specific bias of phase and code on frequency i and j , respectively. \widehat{UPD}_w is the wide-lane UPD estimate with the correction of code OSB, which can be introduced by the IGS ACs products, e.g., WHU, DLR or CAS.

Parameter elimination

Typically, the NEQ associated with the least squares (LSQ) method for orbit determination can be formulated as follows:

$$Nx = W \quad (5)$$

$$\begin{cases} N = A^T P A + P_{x_0} \\ W = P_{x_0} x_0 + A^T P l \end{cases} \quad (6)$$

where x represents the unknowns, initialized with initial values denoted as x_0 , and N is the normal matrix. In addition, W is the right-hand vector of the NEQ, which consists of the closure error of the observations and the a priori parameter, A denotes the design matrix, P and P_{x_0} are the observation weights and parameter constraints, and the vector l is defined as the difference between the observed and computed values, denoted as (O–C). For POD, the estimated parameters x encompass the initial status of orbit, station coordinates, clock biases of stations and satellites, zenith total delay, ambiguities, EOP and UPD. These parameters are categorized into three groups, namely epoch-wise parameters (referred to as EP), piece-wise parameters (referred to as PW), and arc-wise constants (referred to as CONST). The dimension of the normal matrix should be reduced to enhance computational efficiency and minimize storage requirements. The constraints imposed on adjacent epoch-wise (EP) and piece-wise (PW) parameters are expressed with the following pseudo-observations.

$$v_x = x_{k,m} - x_{k,m-1}, p_x = \frac{\sigma_0^2}{p_d^2 \Delta t} \quad (7)$$

where k is the index of the parameter in the NEQ and $x_{k,m}$ and $x_{k,m-1}$ are two consecutive EP or PW active parameters at epochs m and $m-1$, respectively. Besides, p_x is the weight of the constraint, p_d denotes the power density of the process noise, and σ_0^2 represents the a priori unit weight variance. At epoch m , the k^{th} inactivated parameter $x_{k,m-1}$ is expressed and eliminated equivalently as

$$x_{k,m-1} = -\frac{w_k - x_{k,m} + \sum_{l=1; l \neq k}^{n_p} n_{k,l} x_l}{n_{k,k} + p_x} \quad (8)$$

where n_p is the dimension of the NEQ, $n_{k,l}$ is an element of the current normal matrix at k^{th} row and l^{th} column, and w_k is the k^{th} element of the right-hand vector of the normal matrix.

More than half computation time can be saved with inactive parameter elimination. However, with the expanding count of satellites and stations, a significant rise can be observed in the quantity of EP and PW parameters. This increases over 80% of the time allocated to the parameter elimination process. In addition, the data locality causes great concern in algorithm designed for the high-performance computation (HPC) (Quintana-Orti et al. 2008), and the matrix-to-matrix operation should be implied for fast analysis. The order of the parameters within the NEQ is rearranged according to the frequency to be eliminated. Initially, same-type parameters are

grouped together within the NEQ, and subsequently, the three categories of parameters are arranged based on their respective durations, i.e., EPs are listed in the head of the NEQ, following by the PW and CONST parameters. It is noteworthy that, to facilitate the reduction process, ambiguities are positioned at the end of NEQ, despite having a shorter lifespan compared to the CONST parameters, such as station coordinates. Finally, inactive parameters in the NEQ at the current epoch are eliminated at once through a block pattern utilizing matrix operations. Equation (5) is represented as follows by explicitly showing the EP, PW and CONST parameters,

$$\begin{bmatrix} N^{E,E} & N^{E,P} & N^{E,C} \\ N^{P,E} & N^{P,P} & N^{P,C} \\ N^{C,E} & N^{C,P} & N^{C,C} \end{bmatrix} \cdot \begin{bmatrix} x^E \\ x^P \\ x^C \end{bmatrix} = \begin{bmatrix} W^E \\ W^P \\ W^C \end{bmatrix} \quad (9)$$

where the superscripts E , P , and C denote the type of parameters. With the help of HPC libraries deployed in the Central Processing Unit (CPU) and Graphics Processing Unit (GPU) platforms, an efficient resolution of the normal equations is achieved.

EP and PW parameter elimination

Considering the constraint introduced by the process or white noise model among EP parameters in adjacent epochs, Eq. (9) is expressed as

$$\begin{bmatrix} N^{E,E} + P_x & -P_x & N^{E,P} & N^{E,C} \\ -P_x & P_x & 0 & 0 \\ N^{P,E} & 0 & N^{P,P} & N^{P,C} \\ N^{C,E} & 0 & N^{C,P} & N^{C,C} \end{bmatrix} \begin{bmatrix} X_{m-1}^E \\ X_m^E \\ X_m^P \\ X^C \end{bmatrix} = \begin{bmatrix} W^E \\ 0 \\ W^P \\ W^C \end{bmatrix} \quad (10)$$

where X_m and X_{m-1} are the EP parameters in the epoch m and $m-1$, and P_x is the weighting matrix. For convenient extension and elimination, and the parameters at the epoch of $m-1$ are derived as

$$X_{m-1}^E = (N^{E,E} + P_x)^{-1} \cdot (W^E + P_x X_m^E - N^{E,P} X_m^P - N^{E,C} X^C) \quad (11)$$

By removing X_{m-1}^E , the updated normal equations can be obtained and shown in Eq. (12). Moreover, the algorithm is equally effective for handling PW parameters.

$$\begin{aligned} & \left(\begin{bmatrix} P_x & 0 & 0 \\ 0 & N^{P,P} & N^{P,C} \\ 0 & N^{C,P} & N^{C,C} \end{bmatrix} - \begin{bmatrix} -P_x \\ N^{P,E} \\ N^{C,E} \end{bmatrix} [N^{E,E} + P_x]^{-1} \begin{bmatrix} -P_x \\ N^{E,P} \\ N^{E,C} \end{bmatrix}^T \right) \\ & \begin{bmatrix} X_m^E \\ X_m^P \\ X^C \end{bmatrix} = \begin{bmatrix} 0 \\ W^P \\ W^C \end{bmatrix} - \begin{bmatrix} -P_x \\ N^{P,E} \\ N^{C,E} \end{bmatrix} [N^{E,E} + P_x]^{-1} W^E \end{aligned} \quad (12)$$

Ambiguity parameter elimination

Unlike EP and PW parameters, the number of ambiguities fluctuates with each epoch. Normally, only a subset of the ambiguities becomes inactive. Consequently, the deactivated ambiguities should be repositioned to the end of the NEQ for elimination through elementary transformations. Finally, the following normal equations are listed as

$$\begin{bmatrix} N^{E,E} & N^{E,P} & N^{E,C'} & N^{E,A} \\ N^{P,E} & N^{P,P} & N^{P,C'} & N^{P,A} \\ N^{C',E} & N^{C',P} & N^{C',C'} & N^{C',A} \\ N^{A,E} & N^{A,P} & N^{A,C'} & N^{A,A} \end{bmatrix} \begin{bmatrix} X^E \\ X^P \\ X^{C'} \\ X^A \end{bmatrix} = \begin{bmatrix} W^E \\ W^P \\ W^{C'} \\ W^A \end{bmatrix} \quad (13)$$

where the upper scripts A and C' indicate the deactivated ambiguities as well as other constant parameters. Hence, the non-active ambiguities are derived as

$$X^A = (N^{A,A})^{-1} \cdot (W^A - N^{A,E}X^E - N^{A,P}X^P - N^{A,C'}X^{C'}) \quad (14)$$

And Eq. (13) is also updated, and shown with Eq. (15).

$$\left(\begin{bmatrix} N^{E,E} & N^{E,P} & N^{E,C'} \\ N^{P,E} & N^{P,P} & N^{P,C'} \\ N^{C',E} & N^{C',P} & N^{C',C'} \end{bmatrix} - \begin{bmatrix} N^{A,E} \\ N^{A,P} \\ N^{A,C'} \end{bmatrix} (N^{A,A})^{-1} \begin{bmatrix} N^{E,A} \\ N^{P,A} \\ N^{C',A} \end{bmatrix}^T \right) \begin{bmatrix} X^E \\ X^P \\ X^{C'} \end{bmatrix} = \begin{bmatrix} W^E \\ W^P \\ W^{C'} \end{bmatrix} - \begin{bmatrix} N^{A,E} \\ N^{A,P} \\ N^{A,C'} \end{bmatrix} (N^{A,A})^{-1} W^A \quad (15)$$

Parameter recovery

Normally, the recovery of eliminated parameters is performed once all the parameters have been resolved. Hence, the submatrix of the normal matrix should be saved for parameter recovery. For example, $N^{E,E}$, W^E , P_x , $N^{E,P}$ and $N^{E,C'}$ are needed for EP and PW parameters.

Numerical orbit integration

The motion of a satellite under perturbations in a Newtonian physics framework can be described with a second-order differential equation (Montenbruck and Gill 2000). Numerical orbit integration (OI) is an effective method for solving motion equations, and it is widely applied in GNSS POD processing. As the number of satellites increases, the time required for OI also proportionally expands. In OI process, the fundamental step involves computing the right function, alongside the second-order partial derivatives of the state transition matrix and sensitivity matrix. Although the computation efficiency can be enhanced by the larger step sizes and

lower-order integration method, it comes at the expense of diminished accuracy. Therefore, the objective of this study is to enhance the computational efficiency of the right function. This strategy is based on whether the perturbations, or certain components thereof, are time-dependent and free of satellite position. For GNSS satellite POD, these perturbations are common for all satellites during the same orbit period, which are solved only once at the first time. Therefore, these calculations are separated into two parts, namely the satellite location-free (SLF) and satellite location-dependent (SLD) parts, as outlined in Table 1. The four most time-consuming tasks are satellite location calculation (Sat. Loc.), planet location calculation (Pl. Loc.), perturbations coefficient loading (Coef.), and transformation matrix calculation (Trans. Mat.) between the International Terrestrial Reference System (ITRS) and Geocentric Celestial Reference System (GCRS).

Furthermore, multithreading technology is employed to enhance computational efficiency. Three steps are designed in orbit generation, as shown in Fig. 1. Firstly, the initial orbital parameters are prepared by post-fitting the ephemeris of satellites. Afterward, the SLF parts are precalculated for the perturbations. Secondly, multithreading is used to solve the motion equation as well as variation equations based on the numerical integration approach. Finally, the orbits of individual satellites are merged to obtain the output.

Strategies for WUM NRT products

The hourly observations from approximately 120 stations provided by the IGS, the International GNSS Monitoring

Table 1 The dependency of the perturbations on the satellite position for satellite location calculation (Sat. Loc.), planet location calculation (Pl. Loc), coefficient loading (Coef.) and transformation matrix calculation (Trans. Mat.)

Perturbation model	SLD part		SLF part		
	Sat. Loc	Pl. Loc	Coef	Trans. Mat	
N body	•		•		
Gravity	•		•		•
Solid Earth tides	•	•	•		
Ocean tides	•	•	•		
Solid Earth pole tide	•	•	•		
Ocean pole tide	•	•	•		
Relativity	•	•			
Solar radiation pressure	•		•		
Earth radiation pressure	•		•	•	
Thermal radiation	•		•		
Antenna thrust	•				
Atmosphere drag	•		•	•	
Customer model	•				

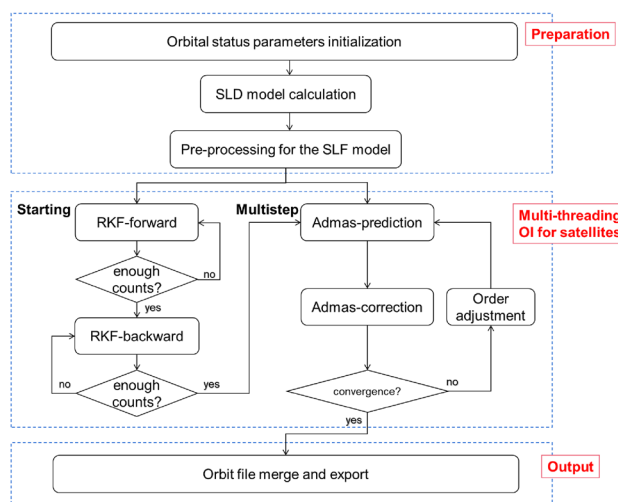


Fig. 1 Flowchart of the modified orbit integration approach with three steps, including preparation, multithreading OI for satellites and output

and Assessment System (iGMAS) (Jiao 2014) and BDS Experimental Tracking Stations (BETS) established by the WHU are utilized. The distribution is illustrated in Fig. 2.

To further reduce computational time, multithreading processing are applied to station- or satellite- independent computations. Figure 3 shows the current workflow for the generation of NRT products at Wuhan University, where the parallel steps are marked in blue. The resolution of double difference (DD) ambiguity fixing is necessary for better estimation of IF ambiguity. Furthermore, the phase OSB is extracted by introducing the WUM code OSB, which can be accessed through ([ftp://igs.gnsswhu.cn/pub/wlu/MGEX/DCB/](http://igs.gnsswhu.cn/pub/wlu/MGEX/DCB/)). Subsequently, the between-satellite single-difference ambiguities are constrained in the NEQ to improve the orbit. Generally, three threads are used for

GPS/GLONASS, GPS/Galileo/QZSS and GPS/BDS combined data analysis to generate the orbit, clock bias, OSB, EOP, and attitude file in orbit exchange format (ORBEX) format (Loyer et al. 2019). In addition, one site with the best data quality among those equipped with an atomic clock is selected as the reference clock. These three POD threads run independently, resulting in an inconsistency among each product. To mitigate this discrepancy, identical stations are employed for the processing. The Galileo, BDS and QZSS orbit, clock, phase OSB, and attitude products from the GPS/Galileo and GPS/BDS combined solutions are extracted and combined with those of the GPS/GLO-NASS solution to obtain the final products. To enhance the orbit prediction precision, a 48-h arc with a sampling rate of 600 s is employed in our analysis, and the orbit will be predicted for the following 24 h to serve as the real-time orbit. The quadratic polynomial model is applied for the clock fitting and predicting. The strategy and parameters of POD processing are summarized in Table 2.

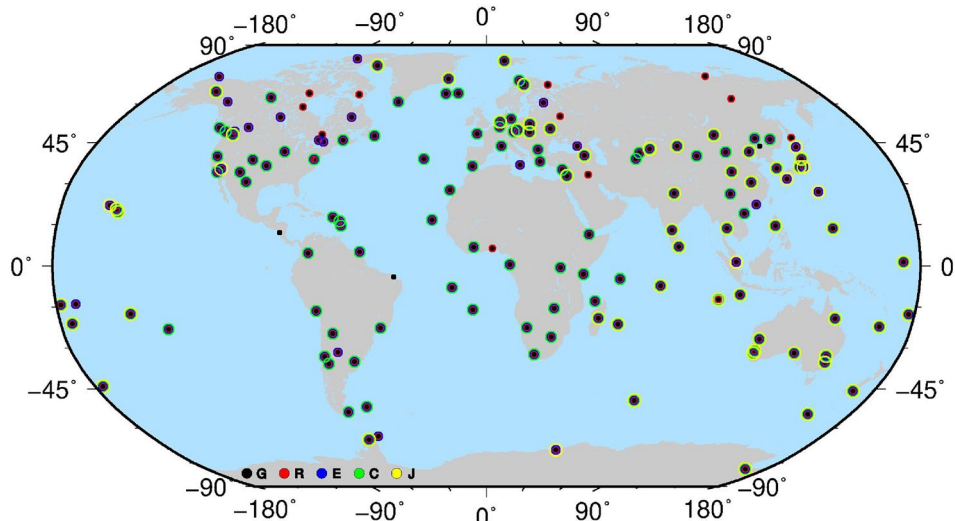
Analysis and assessment

The aforementioned-proposed methods have been implemented in the Position and Navigation Data Analyst (PANDA) software for the WUM NRT multi-GNSS data processing (Liu and Ge 2003).

Efficiency of data processing

Considering data from 120 stations for POD of 120 satellites (32 GPS, 21 GLONASS, 24 Galileo, 40 BDS, and 3 QZSS), the position and velocity of the initial epoch, as well as 7 coefficients of the ECOM-2 model, are estimated for each satellite. Additionally, for each station-satellite

Fig. 2 The distribution of stations used for WUM NRT products on DOY 290, 2023



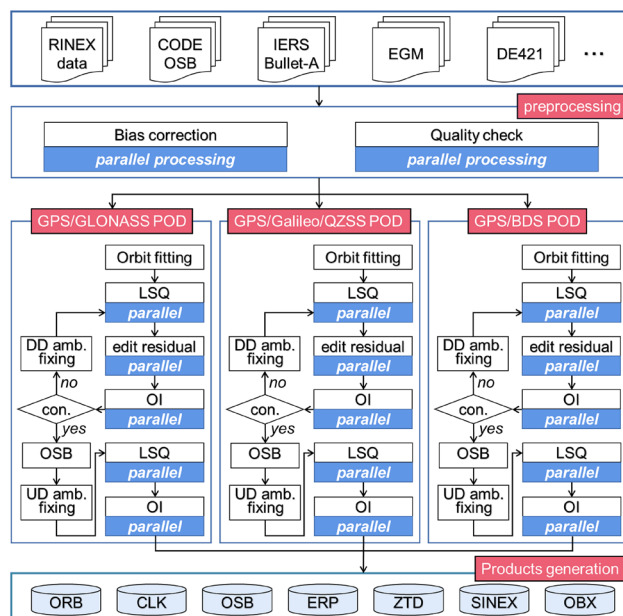


Fig. 3 The workflow for the determination of the WUM NRT products

pair in a 48-h arc, four ambiguity parameters are considered, and the station-specified wet ZTD is estimated hourly. The Inter-system Bias (ISB), Inter-frequency bias (IFB) of GLONASS and EOP are estimated as constants. Table 3 provides a summary of the count and proportions of unknown parameters. The EP and PW parameters constitute approximately 55% of the total, while the ambiguity parameter makes up approximately 42%, with the remaining 3% being other parameters. The EP and PW parameters are linearly correlated with ambiguities, resulting in dominant nonzero elements in the NEQ.

The revised method is compared with the algorithm proposed by Ge et al. (2006), and a server with an 8-core CPU (Intel® Xeon® CPU E5-2667, 2.9 GHz), 128 GB memory and a NVIDIA Tesla P100 GPU is used for the calculation. The GPU is operating at a frequency of 1190 MHz and 3584 Compute Unified Device Architecture (CUDA) cores (1.3 GHz) are equipped with the double-precision performance of about 5.3 Tera floating-point operations per second (TFLOPS). Processing is conducted on both CPU and GPU platforms utilizing HPC libraries. The MKL Intel mathematical library (Intel 2022) is specifically employed for matrix operations on the CPU. In addition, the cuBLAS and cuSOLVER libraries developed by NVIDIA are used for the GPU-based experiments (NVIDIA 2022a, 2022b). The HPC libraries are employed in the linear algebraic operation, as the libraries have been professionally optimized, and the calculation is operated with multithread on CPU and GPU platforms. Figure 4

illustrates the time consumption for LSQ used in PANDA as the number of stations increases.

It should be noted that, the element-by-element operation consumes considerable time for the Ge's method. Linear increase is observed for the revised method, owing to the enhanced efficiency with block operation of NEQ. The right panel of Fig. 4 reveals that the computation time of the CPU-based method is lower than that of GPU-based algorithm when the number of stations is below 35. This discrepancy is attributed to the delay in data transmission between Random-Access (RAM) and the GPU video memory. In this paper, the GPU-based method exhibits improved computational efficiency as the number of stations increases. In the case of 120 stations, the processing time can be diminished by factors of 13 and 29 for the CPU- and GPU-based solutions, respectively.

Besides, numerical orbit integration is another time-intensive step in the POD solution. The following three strategies are employed for the comparative analysis:

Strategy A: sequential method involves the original implementation in PANDA.

Strategy B: sequential method with pre-integration of SLF items for satellites.

Strategy C: parallel integration with pre-integration of SLF items for satellites.

Up to 150 satellites are employed, utilizing the initial orbital elements derived from the broadcast ephemeris. The detailed configuration is presented in Table 2. The time consumption for each procedure of the right function calculation in strategy A is provided in Table 4.

According to the statistical analysis, the computation of SLF items, specifically the transformation between ITRS and GCRS, as well as planet position calculations, accounts for approximately 86% of the total processing time. Furthermore, Fig. 5 disclosed the time consumption associated with the three strategies. Linear variations are observable in all three solutions. However, the slope of strategy A is notably greater than that of the other two strategies. The ratio for strategy B is approximately one-sixth of that for strategy A. A substantial reduction is evident for strategy C with an optimized algorithm and multithreading parallel computation. In general, the time consumption of strategies A, B and C is approximately 149.37 s, 22.72 s and 5.27 s, respectively, considering 120 satellites with a 48-h arc length.

The efficiency for data processing is illustrated in Fig. 6, wherein quality check (QC), LSQ, edit residual (EDTRES) and OI have been optimized for computational efficiency. The efficiency is improved approximately 8 times, enabling the acquisition of ultra-rapid multi-GNSS orbit solutions within 28.5 min for the calculation in our routine processing. Subsequently, the multi-GNSS products can be released on an hourly basis.

Table 2 Strategy and parameters of POD used for data analysis in this study

Item	Description
Observable	Ionosphere-free linear combination based on GPS/QZSS: L1/L2; GLONASS: G1/G2; Galileo: E1/E5a; and BDS: B1I/B3I
POD and prediction length	48 h and 24 h
Sampling	600 s
Output interval for orbit and clock	300 s
Integration step	2 s for RKF and 60 s for Admas
Elevation cutoff angle	7°
Weighting	Elevation-dependent weighting for the observations under 30° according to $1/2 \sin(E)$
Stochastic clock parameter	Random-walk parameter with process noise of $300m/\sqrt{30s}$ and $900m/\sqrt{30s}$ for satellite and receiver
Sat. and Rec. PCO/PCV	IGS igs20.atx antenna model
Ambiguity resolution	Double difference ambiguity fixing (Ge et al. 2006) Undifferenced ambiguity fixing (Geng et al. 2022)
Satellite yaw attitude	GPS (Kouba 2009); GLONASS (Kouba 2013); Galileo (GSA, Accessed 29 Jan. 2024); BDS GEO: orbit nominal mode; BDS-2 C07, C08, C09, C10, C12, C13: yaw-steering and orbit normal mode (Guo et al. 2013). The rest BDS-2 as well as BDS-3 MEO/IGSO CAST satellites (Wang et al. 2018), BDS-3 MEO SECM satellites (Yang et al. 2023)
Geopotential	EGM2008, up to degree and order 12
Solid Earth tides	IERS conventions 2010
Third-body	Sun, Moon, and planets in JPL DE405
SRP model	GPS and GLONASS: Box-wing + ECOM2 (D, Y, B, Bc, Bs, Dc2, Ds2) (Arnold et al. 2015). Galileo: ECOM1 with a priori SRP model (Montenbruck et al. 2015). BDS-2 GEO: 5-parameter ECOM1 with a priori SRP model (Wang et al. 2019). BDS-2 IGSO and MEO: ECOM1 with a constant parameter in the along-track direction (Guo et al. 2016) BDS-3 MEO: ECOM1 with a priori SRP model (Guo et al. 2023)
Empirical acceleration	One constant in the along-track direction
Earth albedo	Rodriguez-Solano et al. (2012)
Antenna thrust	Modified with the method proposed by Steigenberger et al. (2018), and the satellites transmit power are: GPS IIR-A/B: 60 W, IIR-M: 145 W, IIF: 240 W, IIIA: 300 W. GLONASS: 100 W. Galileo IOV: 135 W, FOC 260 W. BDS-2 IGSO: 185 W, MEO: 130 W. BDS-3 MEO-CAST: 310 W, MEO-SECM: 280 W. QZSS-2I: 550 W, 2G 550W, 2A 460W
Relativity	IERS conventions 2010
EOP parameters	Polar motion and UT1 from gprapid.daily series aligned to ITRF2020. Desai-Sibois model for the sub-daily correction
Intersystem bias	One constant parameter per station for Galileo; Two constant parameters per station for BDS-2 and 3
IFB	Frequency-dependent constant parameter for GLONASS

Table 3 Number of parameters for the 48 h POD arc with 120 satellites, 120 stations and a 600 s interval

Parameter	Type	Count	Percentage
Site coordinates	CONST	$120 \times 3 = 360$	0.26%
Satellite initial status	CONST	$120 \times (6+7) = 1560$	1.14%
EOP	CONST	6	0.01%
ISB	CONST	$120 \times 4 = 480$	0.35%
IFB	CONST	$120 \times 14 = 1680$	1.23%
Ambiguity	CONST	$120 \times 120 \times 4 = 57,600$	42.18%
ZTD_{wet}	PW	$120 \times 48 = 5760$	4.21%
Sat. Clock	EP	$120 \times 288 = 34,560$	25.31%
Sit. Clock	EP	$120 \times 288 = 34,560$	25.31%
Total:		136,566	100%

Performance of the WUM NRT products

To assess the orbit quality, GPS and GLONASS orbits are compared with IGS final products, whereas Galileo, BDS and QZSS orbits are compared with the WHU Multi-GNSS Combined (WMC) orbit (Chen et al. 2023). Products from DOY 192 to DOY 297 in 2023 are utilized for the comparative analysis. Considering the distinct characteristics of GEO, IGSO and MEO constellations, the assessment of BDS and QZSS orbit quality is conducted based on the constellation types rather than averaging across all satellites. Figures 7 and 8 show the orbit differences of estimated orbit in along-track, cross-track, radial, and three-dimensional (3D) components.

Fig. 4 Time consumption of LSQ for the original and optimized methods. The Ge method (black square) is originally employed in PANDA. The modifications are M:CPU-based (red point) and M:GPU-based (blue diamond) methods

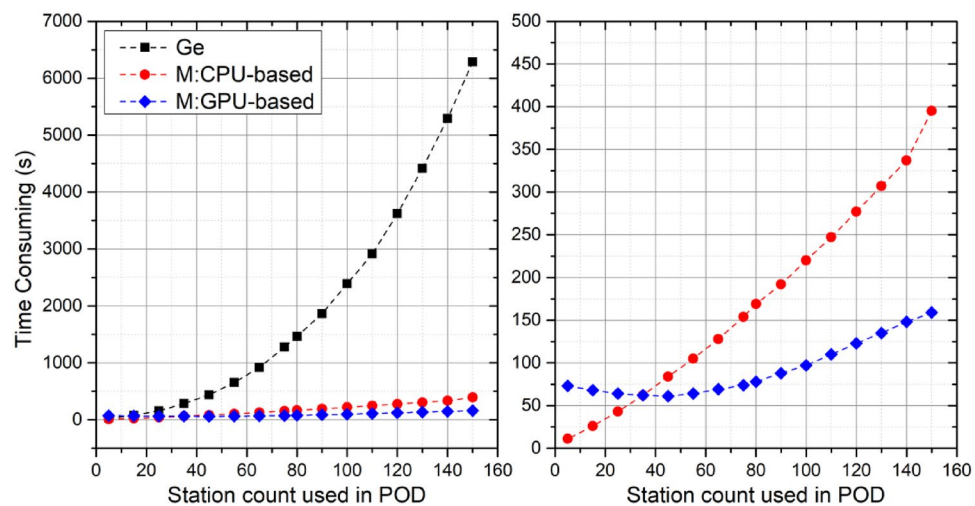


Table 4 Time consumption for the four selected procedures within the computation of the right function for the GNSS satellites

	Time-consuming [ms]	Percentage
Transformation between ITRS and GCRS	2341	56.3
Planet position	1231	29.6
Coefficients of gravitation	462	11.1
Others	125	3.0
Total operation	4158	100

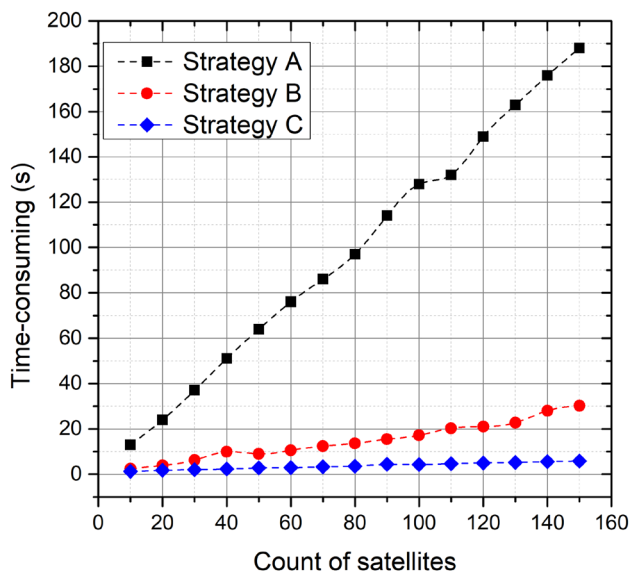


Fig. 5 Time consumption of numerical orbit integration for strategies A (black square), B (red point) and C (blue diamond) with the increasing number of satellites

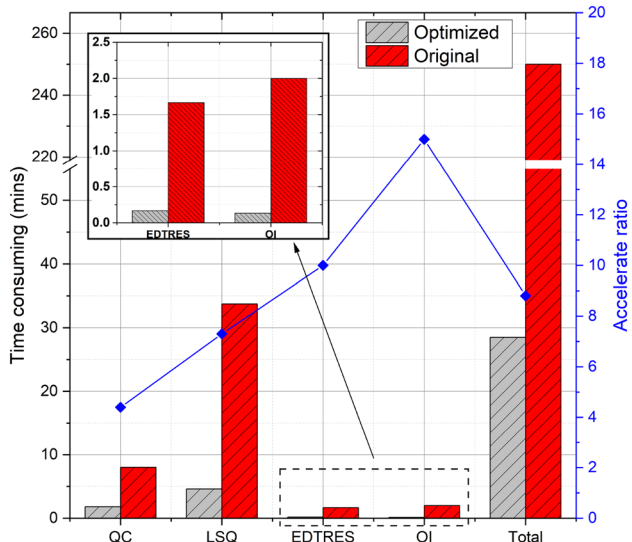


Fig. 6 The time consumption for the generation of NRT products, where the blue diamonds represent the accelerating ratio. QC is used for the precheck of observations; LSQ is the estimator, EDTRES is used for post-fitting the residual, and OI is used for numerical integration

As illustrated in Figs. 7 and 8, the MEO orbits show the best precision, followed by IGSO orbits and GEOs. Concerning MEO satellites, GPS and Galileo demonstrate superior performance, achieving a 3D precision better than 1.9 cm. GLONASS and BDS3-MEO satellites exhibit values within 3.7 cm. In contrast, BDS2-MEO satellites display the orbital differences better than 8.4 cm. The reason is that only three satellites are currently in-orbit and intra-constellation ambiguity fixing is employed for BDS2 and BDS3 for the consideration of the code bias between BDS2 and BDS3 (Steigenberger et al. 2023; Xu and Cai 2023). In the case of IGSO from BDS and QZSS, the 3D precision indicates a consistency within the range from 10.3 to 14.2 cm. However,

Fig. 7 The accuracy of observed parts in hourly NRT orbit products for GPS, GLONASS, Galileo and BDS MEO satellites w.r.t. IGS final (Superscript ‘1’) and WMC orbit (Superscript ‘2’)

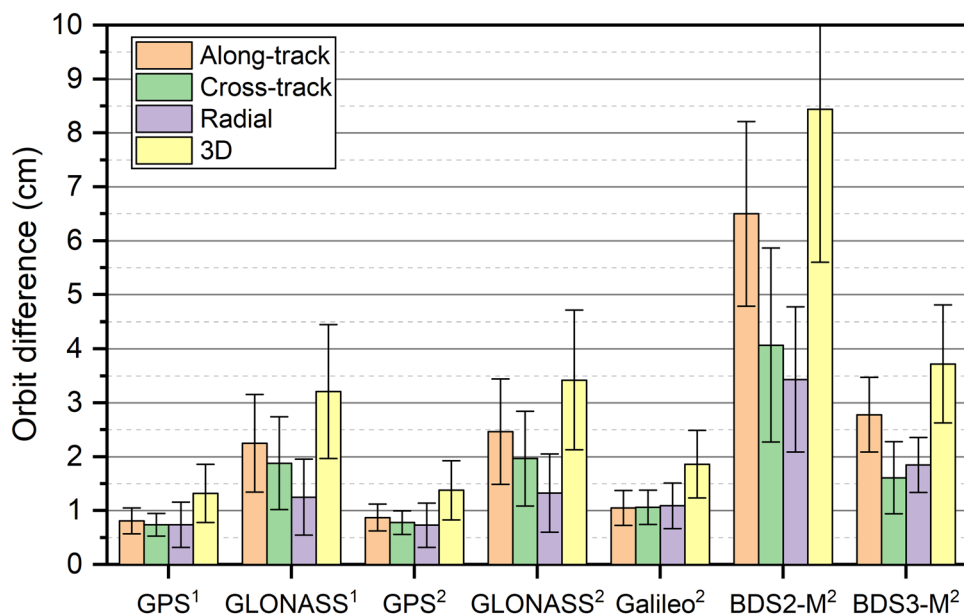
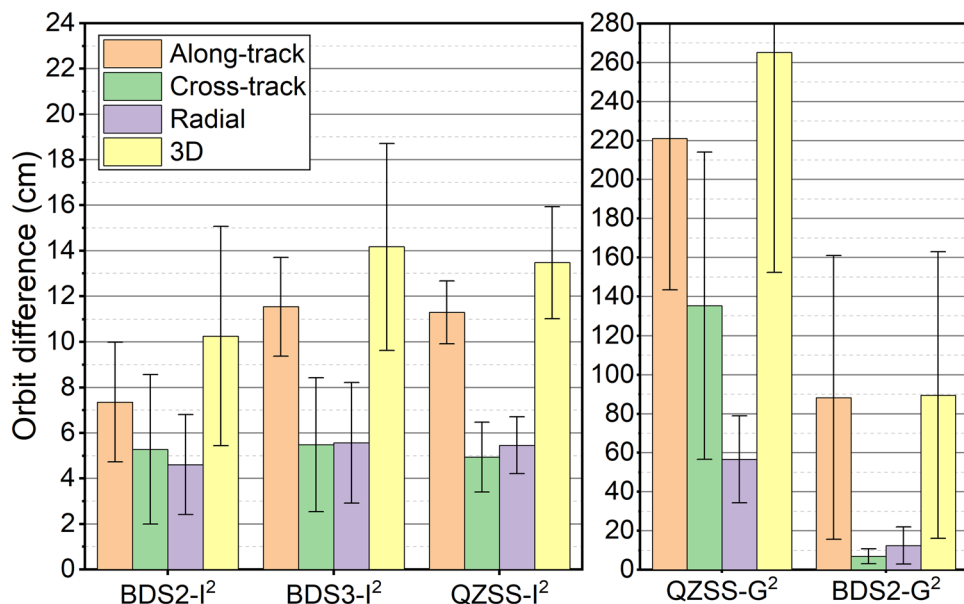


Fig. 8 The accuracy of observed parts of hourly NRT orbit products for BDS and QZSS IGSO and GEO satellites w.r.t. WMC orbit (Superscript ‘2’)



for GEO orbit, the differences show up to 2.65 m for QZSS satellites, due to the imperfect SRP model and static viewing geometry.

In the domain of predicted real-time orbit, the products are released with one-hour latency and one-hour intervals. Our emphasis is the predicted orbit within the first to second hour. Table 5 presents the median values of orbital discrepancies in along-track, cross-track, radial and 3D directions. The MEO satellites of GPS, GLONASS, Galileo and BDS3-MEO show the best performance, with 3D consistency ranging from 2.4 cm to 5.0 cm. For IGSO satellites in BDS and QZSS, the precision varies from 11.4 cm to 15.7 cm, whereas GEO satellites exhibit the

worst performance, with precision ranging from 1 to 3 m. Noted that, as the evolution of orbit and clock quality for CNES CLK93 has been evaluated by Kazmierski et al. (2020), the signal-in-space ranging error (SISRE) for Galileo is lower than that for GPS. The orbital error in the radial direction can be absorbed and compensated with clock, which results in the better precision of SISRE with GPS and Galileo than our orbit-only results.

Figure 9 depicts the cumulative distribution function (CDF) of real-time orbit errors. The CDFs of MEO and IGSO orbits for GPS, Galileo, and QZSS exhibit similar patterns. The 95th-percentile values for the along-track, cross-track and radial components are listed as follows: (5.8, 3.2,

Table 5 The median values of the real-time orbit w.r.t. IGS and WMC orbit products in along-track, cross-track, radial and 3D direction. (Units: mm)

	Along-track	Cross-track	Radial	3D	Reference
GPS	18.6	10.8	9.1	23.5	IGS
GLONASS	37.7	21.9	15.0	46.1	IGL
GPS	18.1	11.3	9.1	23.2	WMC
GLONASS	39.5	23.1	14.9	48.1	WMC
Galileo	32.1	15.2	13.6	38.0	WMC
BDS2-MEO	117.4	48.3	41.5	133.6	WMC
BDS3-MEO	36.9	21.2	24.9	49.5	WMC
BDS2-IGSO	80.1	67.9	65.2	124.0	WMC
BDS3-IGSO	97.2	90.0	83.4	157.2	WMC
BDS2-GEO	683.2	32.5	179.9	709.2	WMC
QZSS-IGSO	55.6	52.1	84.9	114.3	WMC
QZSS-GEO	1338.9	1914.9	222.8	2347.1	WMC

3.0) cm for GPS, (9.7, 4.5, 4.2) cm for Galileo and (16.1, 14.4, 21.4) cm for QZSS. Regarding GLONASS, excluding two satellites, possibly due to the aging of satellite payload (R19 and R20), the 95th-percentile values are (11.8, 6.6, 4.7) cm. For BDS, three distinct patterns emerge. BDS3-MEO exhibits superior performance, with values of (11.2, 5.6, 6.7) cm, followed by BDS2-MEO (33.8, 14.7, 13.9) cm and IGSO satellites(24.4, 19.0, 21.7) cm, respectively.

BDS-3 IGSO exhibits the worst performance, with values at the 95th-percentile of (25.4, 22.1, 27.4) cm. For the BDS3-MEO satellites, notable degradation occurs in C45 and C46, potentially attributed to an inadequate a priori SRP model, which is equipped with Search and Rescue (SAR) payload, and further refinement is needed (Zhao et al. 2022).

GNSS clock can only be estimated relatively. As one site with high stable hydrogen maser (PHM) is set as a reference in this study, the AC-specific clock datum is involved in the clock corrections. For clock assessment, one satellite clock is selected as a datum, and the differences of other satellite clock for specific satellite are formed to remove the system bias. Afterward, the clock of the same satellite pair from IGS and Center for Orbit Determination in Europe (CODE) is further differenced and the Standard Deviation (STDev) of the double-difference clock correction are calculated as indicators of clock quality. NRT clock from DOY 192, 2023 to DOY 297, 2023 are assessed, and the clock correction of GPS is conducted with respect to IGS final clocks, and the rest constellations are compared with CODE final products. The STDevs of observed parts are shown in Fig. 10. For MEO satellites, the mean values are better than 0.1 ns, except for BDS-2. GPS show the best consistency, the next are Galileo, BDS-3 and GLONASS. The STDevs of BDS-2 and QZSS IGSO satellites are about 0.3 ns. BDS-3 IGSO show the worst agreement with approximately 0.6 ns. As the

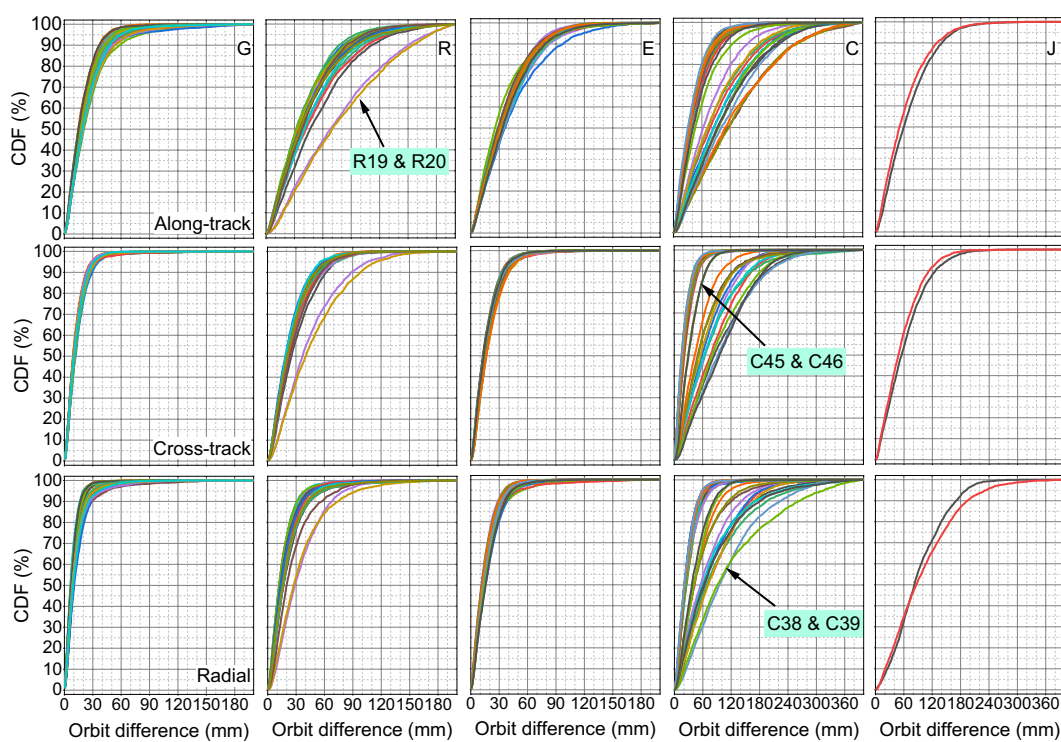


Fig. 9 CDFs of real-time orbit precision for GPS, GLONASS, Galileo, BDS and QZSS IGSO and MEO satellites

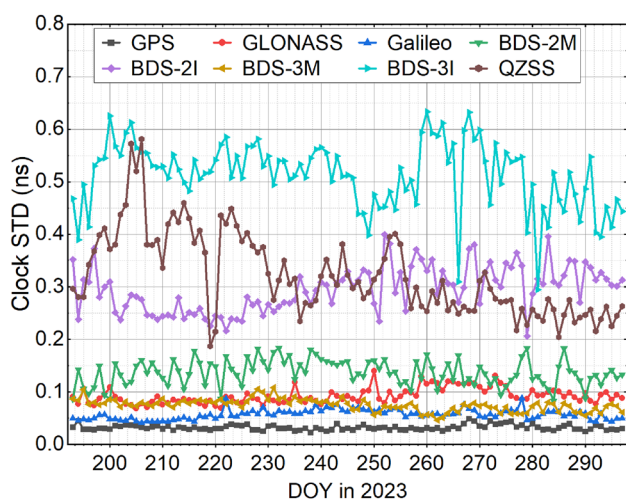


Fig. 10 The STDev of the observed parts clock difference between WUM NRT and IGS/CODE clock products, during DOY 192 to DOY 297, 2023

Table 6 The STDevs of the NRT clock w.r.t. IGS and CODE products. (Units: ns)

	STD	Reference
GPS	0.406	IGS
GLONASS	0.694	CODE
Galileo	0.238	CODE
BDS2-IGSO	0.892	CODE
BDS2-MEO	0.719	CODE
BDS3-IGSO	0.748	CODE
BDS3-MEO	0.189	CODE
QZSS	0.502	CODE

GEO clock are not released by CODE, GEO satellites clock of BDS and QZSS are not illustrated.

In addition, the mean STDevs of NRT clock w.r.t. IGS and CODE final clock products are shown in Table 6. As expected, Galileo and BDS-3 MEO perform the best, which may benefit from the improved performance of onboard PHM and Rubidium Atomic Frequency Standard (RAFS).

PPP-AR with NRT OSB

Phase OSB data spanning DOY 270 to 290, 2023 are employed for the analysis. Figure 11 illustrates the box plot of phase OSB products, focusing on the L1W, L1C, L2I and L2X signals of GPS, Galileo, BDS and QZSS. Mean values are removed for each satellite. The majority of phase OSB values exhibit peak-to-peak variations within 0.5 ns, although exceptions are observed for BDS2-IGSO and MEO satellites.

To validate the accuracy of the NRT products, PPP-AR is conducted for receivers within the IGS network. The open-source software PRIDE PPP-AR is employed (Geng et al. 2019a) in this study. Approximately 340 IGS stations with multi-GNSS observations are included, and positioning results are compared with the IGS weekly coordinate solutions.

Figure 12 shows the distribution of the fractional parts of wide-lane ambiguity for GPS, Galileo, BDS-2 and BDS-3. The proportion of residuals within ± 0.15 cycle, ± 0.20 cycle and ± 0.25 cycle is counted, and more than 95% absolute residual values of wide-lane ambiguity are within 0.25 cycles except for BDS-2, which may be caused by the lower accuracy of BDS-2 code observation. The distribution of narrow-lane residual is displayed in Fig. 13. For the narrow-lane fix rate, only the epoch passed the WL fixing are participated in statistics, and the ratio is calculated by the epoch passed the NL fixing checking and the number of the epoch which has passed the WL fixing checking. The proportion

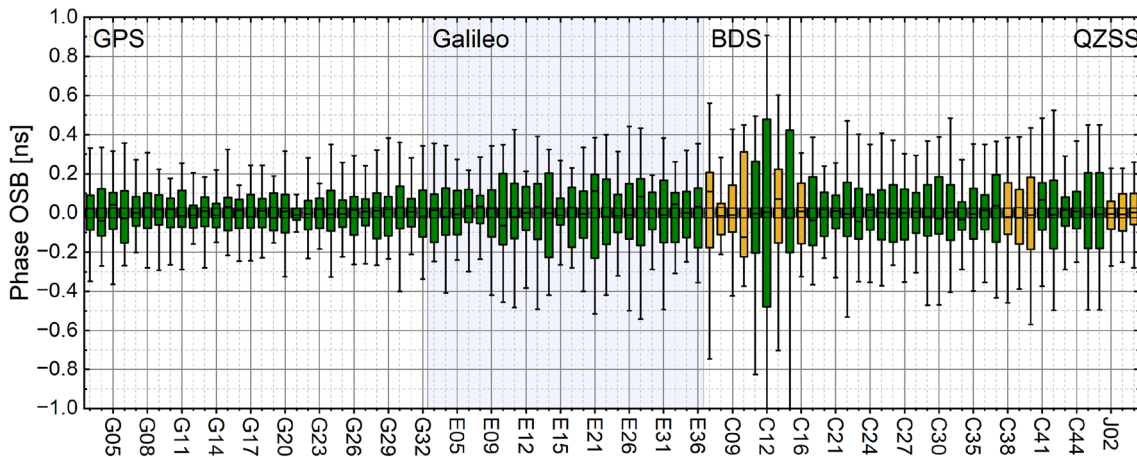


Fig. 11 Statistics of the phase OSBs for GPS, Galileo, BDS and QZSS satellites. The boxes in green colors indicate the MEO satellites, and those in yellow colors represent the IGSO satellites

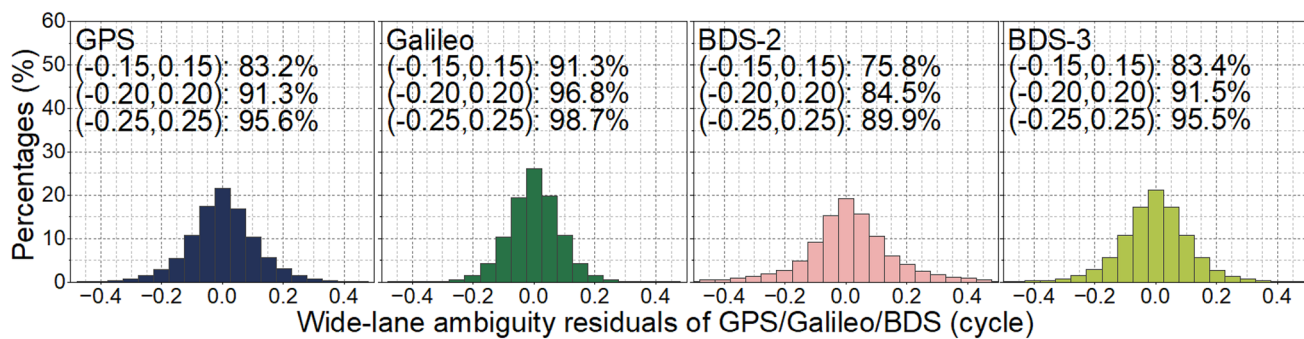


Fig. 12 Residual distributions of wide-lane ambiguity estimation for GPS, Galileo, BDS-2 and BDS-3 satellites with WUM NRT products

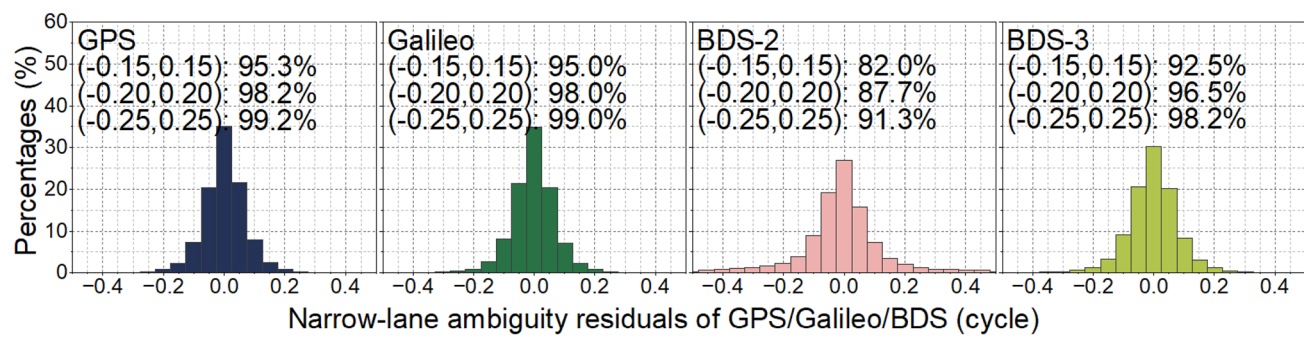


Fig. 13 Residual distributions of narrow-lane ambiguity estimation for GPS, Galileo, BDS-2 and BDS-3 satellites with WUM NRT products

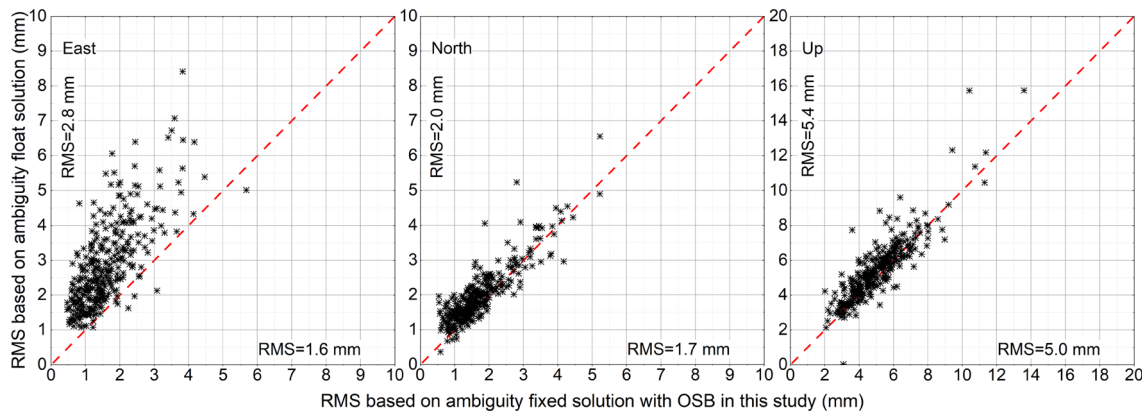


Fig. 14 RMS of static PPP solutions with respect to IGS weekly solutions

of narrow-lane with ± 0.15 cycle is above 95.3%, 95.0% and 92.5% for GPS, Galileo and BDS-3, respectively, while the percentage of BDS-2 is about 82.0%.

The results for east, north, and up direction of the static positioning solutions with respect to IGS weekly solutions are presented in Fig. 14. The decision threshold of 0.2 and 0.15 cycle are set for wide-lane and narrow-lane in this study. To improve the accuracy of the solution, one more iteration of

ambiguity fixing has been carried out, and 3% more narrow-lane fixing rate can be observed. The enhancement is evident in the ambiguity-fixed solution, with mean Root Mean Square (RMS) values measuring 1.6 mm, 1.7 mm, and 5.0 mm for the east, north and up directions, respectively. In addition, the mean wide-lane fixing rate is 91.3%, 96.8%, 84.5% and 91.5% for GPS, Galileo, BDS2 and BDS3. And the narrow-lane fixing rate is 99.4% for GPS, 99.1% for Galileo, 91.3% for BDS2 and

98.1% for BDS3. In general, a higher fixing rate of Galileo is observed, potentially attributed to its enhanced code accuracy in comparison to the legacy signal of GPS and BDS, specifically L1, B1I and B3I.

Conclusions

In this study, the models and strategies employed for the generation of NRT orbit, clock and phase OSB products at Wuhan University are introduced. For enhancing computational efficiency, the parameters within the NEQ are reorganized, and the matrix-to-matrix operations are optimized using the HPC math kernel library. The computational time exhibits notable improvements, achieving factors of 13–29 on the CPU and GPU platform, respectively. The efficiency of the numerical orbit integration algorithm is similarly improved, ranging from 6 to 28 times, through the incorporation of pre-integration and multithreading processing proposed in this contribution. It is promising that only 4.98 s are required to solve the motion equation for 120 GNSS satellites. Ultimately, with the implementation of these optimized strategies, multi-GNSS products of GPS, GLONASS, Galileo, BDS and QZSS can be updated within 28.5 min in our routine processing for a global network comprising 120 tracking stations.

Moreover, NRT products encompassing orbit, clock and dual-frequency phase OSB have been derived. With the benefits of these products, PPP-AR with single station can be accomplished. The estimated orbits exhibit overlapping (3D RMS) w.r.t. IGS and WMC final orbit, with values of 1.4 cm, 3.7 cm, 1.9 cm, and 3.7 cm for GPS, GLOANSS, Galileo and BDS MEO satellites, respectively. In the case of IGSO satellites from BDS and QZSS, the consistency ranges between 6.4 cm and 11.7 cm, while for GEO satellites, the values span from 40.2 cm to 104.7 cm. For real-time available orbits, the median 3D RMS values are 2.4 cm, 4.6 cm, 3.8 cm, and 4.9 cm for MEO satellites, while for IGSO satellites from BDS and QZSS, the median 3D RMS values vary between 11.4 cm and 15.7 cm. Besides, the precision of GEO satellites ranges between 70.9 cm and 234.7 cm. For assessment of clock w.r.t. IGS and CODE final products, the observed-parts consistency of MEO satellite is better than 0.1 ns, except for BDS-2. The STDevs of BDS-2 and QZSS IGSO satellites are about 0.3 ns, and BDS-3 IGSO shows the worst agreement, approximately 0.6 ns. For the real-time available parts, the Galileo and BDS-3 MEO perform the best with 0.2–0.3 ns, which may benefit from the improved performance of onboard PHM and RAFFS. Whereas, it is about 0.4 ns and 0.7 ns for GPS and GLONASS. The consistency of BDS and QZSS IGSOs is about 0.5–0.9 ns.

Finally, the near real-time products are validated through PPP-AR involving 340 globally distributed IGS stations. The wide-lane fixing rates exceed 91.1% for multi-GNSS, while

the narrow-lane fixing rates are approximately 97.0%. The RMS precisions reach about 1.6 mm, 1.7 mm, and 5.0 mm for the east, north and up directions, respectively. As shown in the results, it is confirmed that the products are efficient and effective with reliable precisions.

Acknowledgements The IGS and iGMAS are acknowledged for providing the multi-GNSS observations.

Author contributions X. Xu works on WUM processing, software, writing original draft. J. Li are involved in OSB algorithm and processing, J. Guo proposed the idea, writing, review and editing. C. Yang and J. Li were involved in writing, review and editing. Q. Zhao help in revision.

Funding This study is financially supported by the National Natural Science Foundation of China (42304032, 41974035), Yong Elite Scientists Sponsorship Program by China Association of Science and Technology (2018QNRC001), the Fundamental Research Funds for the Central Universities (2042021kf0065), and China Postdoctoral Science Foundation, (2020M682483).

Data availability The GNSS tracking data and final orbit products are publicly available from IGS data centers, e.g., at the ftp site: <https://gdc.cddis.eosdis.nasa.gov>. The WUM NRT multi-GNSS orbit, clock, ERP and ORBEX as well as WMC final orbit products are openly available by an anonymous user via <https://igs.gnsswhu.cn/pub/gps/products/mgex/> and <https://igs.gnsswhu.cn/pub/whu/MGEX>.

Declarations

Conflict of interest The authors declare no competing interests.

Ethical approval Not applicable.

References

- Arnold D, Meindl M, Beutler G, Dach R, Schaer S, Lutz S, Prange L, Sosnica K, Mervart L, Jaggi A (2015) CODE's new solar radiation pressure model for GNSS orbit determination. *J Geodesy* 89(8):775–791
- Barbu AL, Laurent-Varin J, Perosanz F, Mercier F, Marty J-C (2018) Efficient QR sequential least square algorithm for high frequency GNSS precise point positioning seismic application. *Adv Space Res* 61(1):448–456
- Bertiger W, Bar-Sever Y, Dorsey A, Haines B, Harvey N, Hemberger D, Hefflin M, Lu W, Miller M, Moore AW, Murphy D, Ries P, Romans L, Sibois A, Sibthorpe A, Szilagyi B, Vallisneri M, Willis P (2020) GipsyX/RTGx, a new tool set for space geodetic operations and research. *Adv Space Res* 66(3):469–489
- Blewitt G, Bertiger W, Weiss JP (2010) Ambizap3 and GPS carrier-range: a new data type with IGS applications. In: IGS Workshop 2010, 28 Jun–2 Jul. 2010, Newcastle
- Chen H, Jiang W, Ge M, Wickert J, Schuh H (2014) Efficient high-rate satellite clock estimation for PPP ambiguity resolution using carrier-ranges. *Sens (Basel, Switz)* 14(12):22300–22312
- Chen X, Ge M, Hugentobler U, Schuh H (2022) A new parallel algorithm for improving the computational efficiency of multi-GNSS precise orbit determination. *GPS Solut* 26(3):83
- Chen G, Guo J, Geng T, Zhao Q (2023) Multi-GNSS orbit combination at Wuhan University: strategy and preliminary products. *J Geodesy* 97(5):41

- Choi K, Ray J, Griffiths J, Bae T (2013) Evaluation of GPS orbit prediction strategies for the IGS Ultra-rapid products. *GPS Solut* 17(3):403–412
- Collins P, Bisnath S, Lahaye F, Héroux P (2010) Undifferenced GPS ambiguity resolution using the decoupled clock model and ambiguity datum fixing. *Navigation* 57(2):123–135
- Dai X, Lou Y, Dai Z, Qing Y, Li M, Shi C (2019) Real-time precise orbit determination for BDS satellites using the square root information filter. *GPS Solutions* 23(2):45
- Deng Z, Wang J, Ge M (2022) The GBM rapid product and the improvement from undifferenced ambiguity resolution. *Acta Geod Et Cartogr Sin* 51(4):12
- Deng Z, Fritsche M, Nischan T, Bradke M (2016) Multi-GNSS ultra-rapid orbit-, clock- & EOP-product series. GFZ data services.
- Dong DN, Bock Y (1989) Global positioning system network analysis with phase ambiguity resolution applied to crustal deformation studies in California. *J Geophys Res Solid Earth Planets* 94(B4):3949–3966
- Duan B, Hugentobler U, Selmeke I (2019) The adjusted optical properties for Galileo/BeiDou-2/QZS-1 satellites and initial results on BeiDou-3e and QZS-2 satellites. *Adv Space Res* 63(5):1803–1812
- Ge M, Gendt G, Dick G, Zhang FP, Rothacher M (2006) A new data processing strategy for huge GNSS global networks. *J Geodesy* 80(4):199–203
- Ge M, Gendt G, Rothacher M, Shi C, Liu J (2008) Resolution of GPS carrier-phase ambiguities in precise point positioning (PPP) with daily observations. *J Geodesy* 82(7):389–399
- Geng J, Chen X, Pan Y, Mao S, Li C, Zhou J, Zhang K (2019a) PRIDE PPP-AR: an open-source software for GPS PPP ambiguity resolution. *GPS Solut* 23(4):91
- Geng J, Chen X, Pan Y, Zhao Q (2019b) A modified phase clock/bias model to improve PPP ambiguity resolution at Wuhan University. *J Geodesy* 93(10):2053–2067
- Geng J, Zhang Q, Li G, Liu J, Liu D (2022) Observable-specific phase biases of Wuhan multi-GNSS experiment analysis center's rapid satellite products. *Satellite Navig* 3(1):23
- Gong XP, Gu SF, Lou YD, Zheng F, Ge MR, Liu JN (2018) An efficient solution of real-time data processing for multi-GNSS network. *J Geodesy* 92(7):797–809
- GSA. (2024). Galileo satellite metadata. <https://www.gsc-europa.eu/support-to-developers/galileo-satellite-metadata>. Accessed 29 Jan 2024
- Guo J, Xu X, Zhao Q, Liu J (2016) Precise orbit determination for quad-constellation satellites at Wuhan University: strategy, result validation, and comparison. *J Geodesy* 90(2):143–159
- Guo J, Wang C, Chen G, Xu X, Zhao Q (2023) BDS-3 precise orbit and clock solution at Wuhan University: status and improvement. *J Geodesy* 97(2):15
- Guo J, Zhao Q, Geng T, Su X, Liu J (2013) Precise orbit determination for COMPASS IGSO satellites during yaw maneuvers. In: China satellite navigation conference (CSNC), 15–17 May 2013, Wuhan
- Herring T (2004) Aspects of large station networks for GPS orbits and clocks. In: Proceedings of IGS workshop and symposium, 1–6 Mar. 2004, Berne
- Intel (2022) Developer reference for Intel® oneAPI math kernel library—Fortran. <https://www.intel.com/content/www/us/en/develop/documentation/onemkl-developer-reference-fortran/top.html>. Accessed 18 Apr 2022
- Jiao W (2014) International GNSS monitoring and assessment system (iGMAS) and latest progress. In: China satellite navigation conference (CSNC), 21–23 May 2014, Nanjing
- Kazmierski K, Sośnicka K, Hadas T (2018) Quality assessment of multi-GNSS orbits and clocks for real-time precise point positioning. *GPS Solut* 22(1):11
- Kazmierski K, Zajdel R, Sośnicka K (2020) Evolution of orbit and clock quality for real-time multi-GNSS solutions. *GPS Solut* 24(4):111
- Kouba J (2009) A simplified yaw-attitude model for eclipsing GPS satellites. *GPS Solut* 13(1):1–12
- Kouba J (2013) A note on the December 2013 version of the eclips. f subroutine
- Laurichesse D, Mercier F, Berthias JP, Broca P, Cerri L (2009) Integer ambiguity resolution on undifferenced GPS phase measurements and its application to ppp and satellite precise orbit determination. *Navigation* 56(2):135–149
- Li L, Lu Z, Cui Y, Wang Y, Huang X (2017) Parallel resolution of large-scale GNSS network un-difference ambiguity. *Adv Space Res* 60(12):2637–2647
- Li X, Chen X, Ge M, Schuh H (2019) Improving multi-GNSS ultra-rapid orbit determination for real-time precise point positioning. *J Geodesy* 93(1):45–64
- Liu J, Ge M (2003) PANDA software and its preliminary result of positioning and orbit determination. *Wuhan Univ J Nat Sci* 8(2):603–609
- Lou Y, Dai X, Gong X, Li C, Qing Y, Liu Y, Peng Y, Gu S (2022) A review of real-time multi-GNSS precise orbit determination based on the filter method. *Satell Navig* 3(1):15
- Loyer S, Montenbruck O, Hilla S (2019) ORBEX: the orbit exchange format, draft version 0.09. <https://geodesy.noaa.gov/pub/ORBEX/ORBEX009.pdf>. Accessed 6 May 2019
- Lutz S, Beutler G, Schaer S, Dach R, Jäggi A (2016) CODE's new ultra-rapid orbit and ERP products for the IGS. *GPS Solut* 20(2):239–250
- Männel B, Brandt A, Nischan T, Brack A, Sakic P, Bradke M (2020) GFZ ultra-rapid product series for the IGS. V. 1.1. GFZ Data Services
- Mayer-Gürr T, Behzadpour S, Eicker A, Ellmer M, Koch B, Krauss S, Pock C, Rieser D, Strasser S, Süßer-Rechberger B, Zehentner N, Kvas A (2021) GROOPS: A software toolkit for gravity field recovery and GNSS processing. *Comput Geosci* 155:104864
- Melbourne WG (1985) The case for ranging in GPS-based geodetic systems. In: First international symposium on precise positioning with the Global Positioning System, Rockville, US, pp 373–386
- Montenbruck O, Gill E (2000) Satellite orbits: models, methods and applications. Springer Verlag, Berlin
- Montenbruck O, Steigenberger P, Hugentobler U (2015) Enhanced solar radiation pressure modeling for Galileo satellites. *J Geodesy* 89(3):283–297
- Nowak A, Zajdel R, Sośnicka K (2023) Optimization of orbit prediction strategies for GNSS satellites. *Acta Astronaut* 209:132–145
- NVIDIA (2022a) cuSOLVER library user guide. https://docs.nvidia.com/cuda/pdf/CUSOLVER_Library.pdf. Accessed 18 Apr 2022
- NVIDIA (2022b) NVIDIA, cuBLAS library user guide. https://docs.nvidia.com/cuda/pdf/CUBLAS_Library.pdf. Accessed 18 Apr 2022
- Prange L, Orliac E, Dach R, Arnold D, Beutler G, Schaer S, Jäggi A (2016) CODE's five-system orbit and clock solution—the challenges of multi-GNSS data analysis. *J Geodesy* 91(4):345–360
- Quintana-Orti G, Quintana-Orti ES, Chan E, Geijn RArd, Zee FGV (2008) Scheduling of QR factorization algorithms on SMP and Multi-core architectures. In: 16th Euromicro conference on parallel, distributed and network-based processing (PDP 2008), 13–15 February 2008. Toulouse, France, pp 301–310
- Rodriguez-Solano CJ, Hugentobler U, Steigenberger P, Lutz S (2012) Impact of Earth radiation pressure on GPS position estimates. *J Geodesy* 86(5):309–317
- Schaer S (2016) SINEX BIAs-solution (software/technique) INDependent EXchange Format for GNSS BIAses Version 1.00. In: IGS workshop on GNSS biases, Bern
- Śliwińska J, Kur T, Wińska M, Nastula J, Dobslaw H, Partyka A (2022) Second earth orientation parameters prediction

- comparison campaign (2nd EOP PCC): overview. *Artif Satell* 57(s1):237–253
- Springer TA, Hugentobler U (2001) IGS ultra rapid products for (near-) real-time applications. *Phys Chem Earth Part A* 26(6):623–628
- Steigenberger P, Thoelert S, Montenbruck O (2018) GNSS satellite transmit power and its impact on orbit determination. *J Geodesy* 92(6):609–624
- Steigenberger P, Deng Z, Guo J, Prange L, Song S, Montenbruck O (2023) BeiDou-3 orbit and clock quality of the IGS Multi-GNSS pilot project. *Adv Space Res* 71(1):355–368
- Steigenberger P, Rothacher M, Dietrich R, Fritzsche M, Rülke A, Vey S (2006) Reprocessing of a global GPS network. *J Geophys Res Solid Earth* 111(B5)
- Takasu T (2013) Development of multi-GNSS orbit and clock determination software. In: The 5th Asia Oceania regional workshop on GNSS, 1–3 December 2013, Hanoi
- Tan B, Yuan Y, Ai Q, Zha J (2022) Real-time multi-GNSS precise orbit determination based on the hourly updated ultra-rapid orbit prediction method. *Remote Sens* 14(17):4412
- Tang L, Wang J, Zhu H, Ge M, Xu A, Schuh H (2023) Multi-GNSS ultra-rapid orbit determination through epoch-parallel processing. *J Geodesy* 97(11):99
- Wang C, Guo J, Zhao Q, Liu J (2018) Yaw attitude modeling for BeiDou I06 and BeiDou-3 satellites. *GPS Solut* 22(4):117
- Wang C, Guo J, Zhao QL, Liu JN (2019) Empirically derived model of solar radiation pressure for BeiDou GEO satellites. *J Geodesy* 93(6):791–807
- Xu X, Cai Z (2023) Characteristics of inter-system bias between BDS-2 and BDS-3 and Its Impact on BDS orbit and clock solutions. *Remote Sens* 15(24):5659
- Yang C, Guo J, Zhao QL (2023) Yaw attitudes for BDS-3 IGSO and MEO satellites: estimation, validation and modeling with intersatellite link observations. *J Geod* 97(1):6
- Zhao Q, Guo J, Wang C, Lyu Y, Xu X, Yang C, Li J (2022) Precise orbit determination for BDS satellites. *Satell Navig* 3(1):2

Publisher's Note Springer Nature remains neutral with regard to jurisdictional claims in published maps and institutional affiliations.

Springer Nature or its licensor (e.g. a society or other partner) holds exclusive rights to this article under a publishing agreement with the author(s) or other rightsholder(s); author self-archiving of the accepted manuscript version of this article is solely governed by the terms of such publishing agreement and applicable law.



Xiaolong Xu received the B.S. degree in Geomatics Engineering from Central South University, Changsha, China, in 2011, and the Ph.D. degree in Geodesy and Surveying Engineering from Wuhan University, Wuhan, China, in 2019. He is currently a postdoctoral researcher at Wuhan University. His current research focuses on dynamic and geometric model of GNSS satellite orbit determination.



Junqiang Li received the B.S. degree in Geodesy and Surveying Engineering from Wuhan University, Wuhan, China, in 2022. His main research interest is GNSS precise orbit determination.



Jing Guo received Ph.D. degree in Geodesy and Surveying Engineering from Wuhan University, Wuhan, China, in 2014. He is currently a professor of GNSS Research Center of Wuhan University. He works on the precise orbit determination for multi-GNSS satellites.



Chao Yang received the PhD. degree in Geodesy and Surveying Engineering from Wuhan University, Wuhan, China, in 2024. His field of work focuses on precise orbit determination for BDS satellites.



Qile Zhao received the Ph.D. degree from Wuhan University, Wuhan, China, in 2004 from Institute of Geology. He is currently a professor of GNSS Research Center of Wuhan University, and his current research interests are precise orbit determination of GNSS and LEO satellites, and high-precision positioning using multi-GNSS.